



Determining the Elemental and Isotopic Composition of the Pre-solar Nebula from *Genesis* Data Analysis: The Case of Oxygen

J. Martin Laming¹ , V. S. Heber², D. S. Burnett³, Y. Guan³, R. Hervig⁴, G. R. Huss⁵, A. J. G. Jurewicz⁴, E. C. Koeman-Shields⁵, K. D. McKeegan², L. R. Nittler⁶ , D. B. Reisenfeld⁷ , K. D. Rieck⁸, J. Wang⁶ , R. C. Wiens⁸, and D. S. Woolum⁹

¹ Space Science Division, Naval Research Laboratory, Code 7684, Washington, DC 20375, USA; laming@nrl.navy.mil

² Dept. of Earth, Planetary & Space Sciences UCLA, Los Angeles, CA 90095, USA

³ Div. of Geological & Planetary Sciences, Caltech, Pasadena, CA 91125, USA

⁴ School of Earth & Space Exploration, Arizona State University, Tempe, AZ 85287, USA

⁵ Hawaii Institute of Geophysics & Planetology, University of Hawaii at Manoa, 1680 East-West Road, Honolulu, HI 96822, USA

⁶ Department of Terrestrial Magnetism, Carnegie Institution of Washington, Washington, DC 20015, USA

⁷ Department of Physics, University of Montana, Missoula, MT 59812, USA

⁸ Space and Remote Sensing (ISR-2), LANL, Los Alamos, NM 877545, USA

⁹ Department of Physics, CSUF, Fullerton, CA 92831, USA

Received 2017 August 29; revised 2017 October 30; accepted 2017 November 20; published 2017 December 6

Abstract

We compare element and isotopic fractionations measured in bulk solar wind samples collected by NASA's *Genesis* mission with those predicted from models incorporating both the ponderomotive force in the chromosphere and conservation of the first adiabatic invariant in the low corona. Generally good agreement is found, suggesting that these factors are consistent with the process of solar wind fractionation. Based on bulk wind measurements, we also consider in more detail the isotopic and elemental abundances of O. We find mild support for an O abundance in the range 8.75–8.83, with a value as low as 8.69 disfavored. A stronger conclusion must await solar wind regime-specific measurements from the *Genesis* samples.

Key words: solar wind – Sun: abundances – Sun: chromosphere – turbulence – waves

1. Introduction

Solar system bodies formed from the pre-solar nebula, but at different places, at different times, and through different processes. Variations in their elemental and isotopic compositions observed today give clues to the mechanisms of formation of these different bodies. A major problem has been our lack of knowledge of the original composition of the solar nebula. Although the Sun represents 99.86% of the known mass of the solar system, its elemental composition revealed by remotely sensed spectroscopy of its photosphere is not determined with sufficient precision to meet planetary science needs, and its isotopic composition is hardly known at all.

NASA's *Genesis* mission (Burnett 2013; Burnett et al. 2017) was designed to solve these problems by collecting samples of solar wind which were then returned to Earth for analysis in laboratory mass spectrometers at far higher precision and better calibration than can be achieved in flight. *Genesis* orbited the L1 Lagrange Point between 2001 December 3 and 2004 April 1, collecting solar wind ions in various different collector materials. Despite the setback caused by the crash of the Sample Return Capsule upon return to Earth, high-accuracy element abundance results now exist for bulk solar wind samples for over a dozen elements. Additionally, isotopic abundances have been measured in the bulk solar wind for N, O, He, Ne, Ar, Kr, and Xe, and isotopic fractionation between fast and slow solar wind regimes has been measured for a subset of these elements (He, Ne, Ar).

This suite of data represents an opportunity to compare precise and accurate solar wind composition with that of the underlying solar composition. Elemental fractionation between the solar photosphere and corona and wind has been known since 1963 (Pottasch 1963). Elements with first ionization potential (FIP) below about 10 eV (e.g., Mg, Si, Fe;

those that are predominantly ionized in the solar chromosphere) are seen to be enhanced in abundance in the corona by a factor of about 3–4 relative to the so-called high FIP elements (e.g., H, O, Ar), which are mainly neutral below the corona. Similar fractionation is seen in the solar wind, although it varies with solar wind regime; the fast wind is less fractionated in this manner than the slow speed wind (e.g., Bochsler 2007a; Pilleri et al. 2015).

This FIP fractionation is now understood as being due to the action of the ponderomotive force (Laming 2004, 2009, 2012, 2015, 2017). This arises as magnetohydrodynamic waves propagate through, or reflect from, the solar chromosphere. If, as recent observations suggest (e.g., De Pontieu et al. 2007), these waves carry significant energy and momentum in the solar atmosphere, then any change in their direction of propagation due to density gradients in the Sun must result in a consequential net force on the plasma. Because the waves of interest here are fundamentally oscillations of the magnetic field (Alfvén and fast mode waves, collectively known as "Alfvénic" when close to parallel propagation), they only interact with the ionized fraction of the plasma. Hence, the ponderomotive force separates ions from neutrals.

The FIP fractionation, including the depletion of He, is most faithfully reproduced in a model of a closed coronal loop where the Alfvén waves are resonant (Laming 2012, 2017; Rakowski & Laming 2012), so that the coronal loop acts as a resonant cavity, where the Alfvén wave travel time from one footpoint to the other is an integral number of wave half-periods. Although it is possible for waves ultimately deriving from convection within the solar envelope to enter coronal loops at footpoints and propagate into the corona, typically the periods of these waves (three or five minutes) are too long for resonance. Resonant waves are most plausibly excited

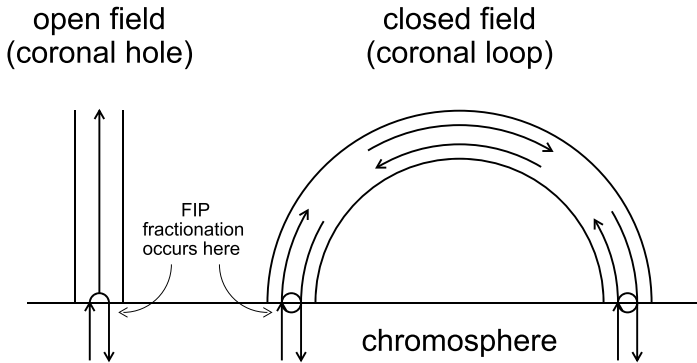


Figure 1. Left: schematic showing FIP fractionation in open and closed field regions. In both cases, waves impinge on footpoints from below, but the closed field can also have wave generation within the corona. Right: model element fractionation in open (top, shifted up by 0.5 for clarity) and closed field (bottom). The result shown here is for model 1 (see Table 1). Short green dashed lines show ponderomotive acceleration only; long purple dashed lines show the combined effect of ponderomotive acceleration and adiabatic invariant conservation. The inset shows the region around H, O, Kr, and N in more detail, for fast wind (top) and slow wind (bottom), for the combined model only. Note that the fractionation ratio O/H > 1 in the slow wind, but is < 1 in the fast wind.

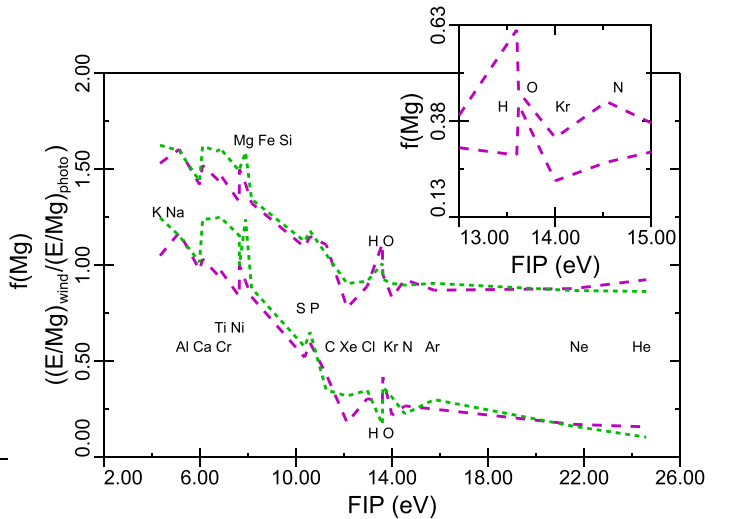
within the coronal loop itself, most likely as a byproduct of the mechanism(s) that heat the corona (Dahlburg et al. 2016). In open field regions, such a resonance does not exist, and only waves propagating up from footpoints are possible. In such a scenario, the difference in fractionation between fast wind, which originates in open magnetic field structures on the Sun, and slow wind, which originates in closed coronal loops that are subsequently opened up by interchange reconnection (e.g., Lynch et al. 2014), arises naturally due to the extra resonant waves. Figure 1 (left panel) gives a schematic illustration of the open and closed field models, and the right panel illustrates the different fractionation patterns (see below for fuller discussion).

2. Model Calculations

The fractionation is calculated in each case by solving Alfvén wave transport equations in a model coronal structure. In the open field region, a spectrum of Alfvén waves is chosen to match those given in Cranmer & van Ballegooijen (2005) and Cranmer et al. (2007) high up in the corona, and integrated back to the chromosphere. In the closed loop, we take a single Alfvén wave corresponding to the fundamental of a 75,000 km long loop having a 10 G coronal magnetic field, combined with two additional photospheric waves with periods of three and five minutes (e.g., Heggland et al. 2011). All of the waves are taken to be shear (planar) Alfvén waves (Laming 2017). The instantaneous ponderomotive acceleration, a , is given by

$$a = \frac{c^2}{2} \frac{\partial}{\partial z} \left(\frac{\delta E^2}{B^2} \right) \quad (1)$$

where δE is the wave electric field, B is the ambient magnetic field, c is the speed of light, and z is a coordinate along the magnetic field. The element fractionation, f_p , is calculated from the ratio of densities ρ_k for element k at upper and lower boundaries of the fractionation region z_u and z_l , respectively, as



given by the equation (Laming 2017)

$$f_p = \frac{\rho_k(z_u)}{\rho_k(z_l)} = \exp \left\{ \int_{z_l}^{z_u} \frac{2\xi_k a \nu_{kn}/[\xi_k \nu_{kn} + (1 - \xi_k) \nu_{ki}] dz}{2k_B T/m_k + v_{||,osc}^2 + 2u_k^2} \right\}, \quad (2)$$

where ξ_k is the element ionization fraction, ν_{ki} and ν_{kn} are collision frequencies of ions and neutrals with the background gas (mainly hydrogen and protons), $k_B T/m_k (=v_z^2)$ represents the square of the element thermal velocity along the z -direction, u_k is the upward flow speed, and $v_{||,osc}$ is a longitudinal oscillatory speed, corresponding to upward and downward propagating sound waves. Because $\nu_{ki} \gg \nu_{kn}$ in the fractionation region at the top of the chromosphere, small departures of ξ_k from unity can result in large decreases in the fractionation.

Isotopic fractionation between fast and slow solar wind has also been observed in the *Genesis* data. Specifically, lighter isotopes are more abundant relative to heavy ones of the same element in the slow wind as compared to the fast (Heber et al. 2012a). This is the opposite of what would be expected from Equation (2), where with increased ponderomotive acceleration, a , a heavier isotope would have a smaller thermal speed and hence a higher value of f_p . An extra mass dependent fractionation (MDF) mechanism must be present. Inefficient Coulomb drag (ICD) has frequently been discussed, especially in connection with the depletion of He in the solar wind (Bodmer & Bochsler 1998; Bochsler 2007b). This depletion is now part of the FIP fractionation. During the *Genesis* data collection period, there is little other evidence for ICD in data collected by *Genesis*, *Wind* (Kasper et al. 2012), or the *Advanced Composition Explorer* (*ACE*; Pilleri et al. 2015) in element abundances (the solar minimum of 2007–8 might be a different matter). ICD should be strongest in the fast wind emanating along open field lines in coronal holes, with slow wind originating in closed loops more fully mixed by waves and turbulence; this is the opposite of what we see.

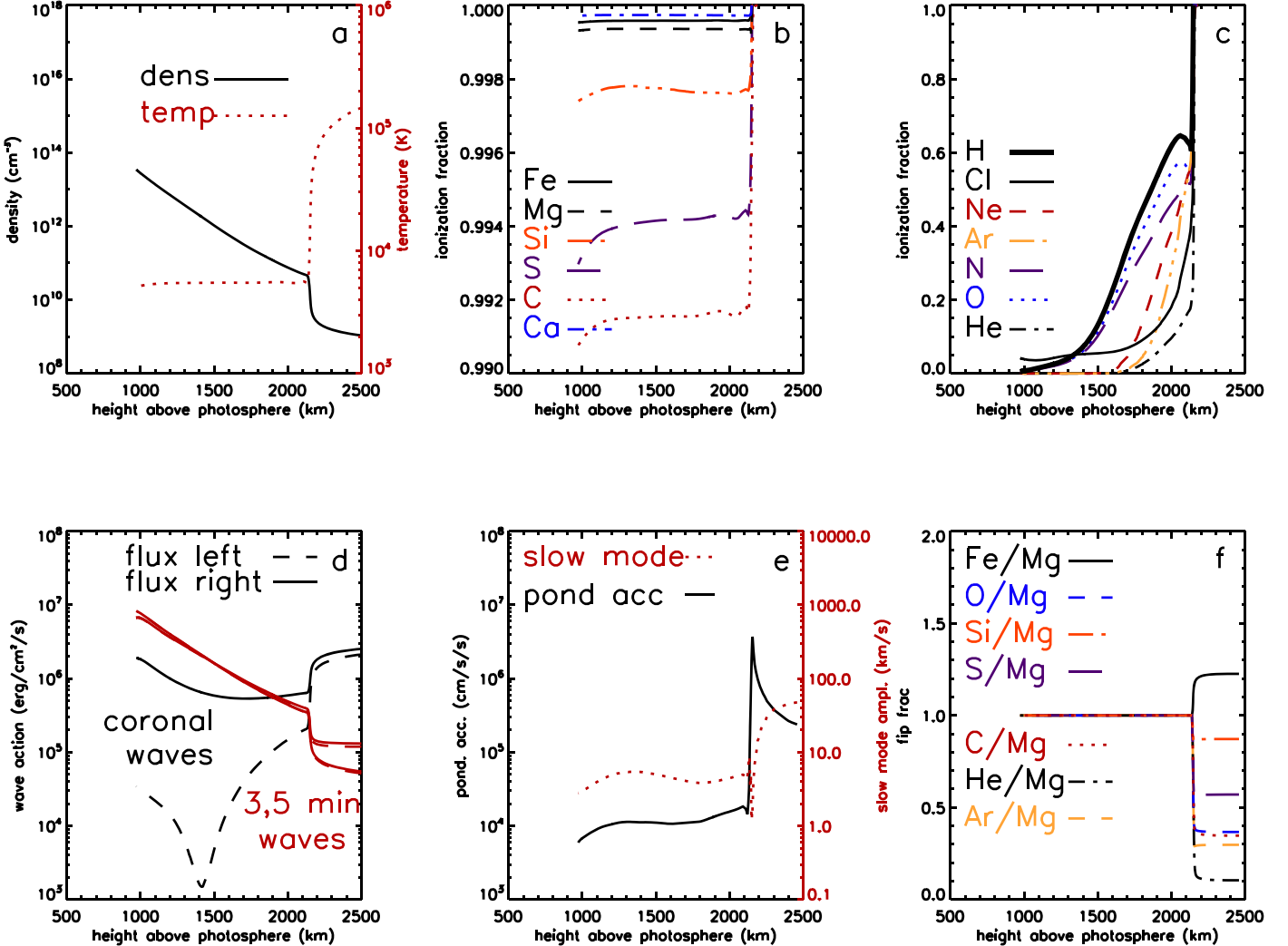


Figure 2. Chromospheric model. (a) shows the density and temperature structure of the chromosphere. (b) shows chromospheric ionization fractions for low FIP elements and (c) for high FIP elements. (d) shows the wave energy fluxes in each direction for the three waves in the closed loop model. (e) shows the ponderomotive acceleration (solid line) and the amplitude of slow mode waves induced by the Alfvén wave driver. (f) shows the fractionations resulting for selected elements relative to Mg. Gas pressure and magnetic field pressure are equal at about 1000 km, with magnetic field pressure dominating at higher altitudes.

We argue, therefore, that the MDF of isotopes is most likely due to the conservation of the first adiabatic invariant, in conditions where the ion gyrofrequency $\Omega = eB/m_k c \gg 1/\tau_{\text{coll}} \gg v_{\text{ex}}/R$. The first inequality means that an ion executes many gyro-orbits around the magnetic field line in the time between Coulomb collisions with other ions, τ_{coll} , and thus the magnetic flux enclosed by its orbit is conserved. Hence, $B r_g^2 \propto (v_x^2 + v_y^2)/B = v_{\perp}^2/B$ is constant (r_g is the particle gyroradius), giving rise to an acceleration

$$\frac{dv_z}{dt} = -\frac{1}{2} \frac{dB}{dz} \frac{v_{\perp}^2}{B} \quad (3)$$

in conditions where $v^2 = v_z^2 + v_{\perp}^2$ is constant. The second inequality expresses the condition that the plasma remain otherwise *collisional*, in that Coulomb collision frequencies are much greater than the expansion rate (wind speed, v_{ex} , divided by radius, R) of the solar wind, and local abundance enhancements in the corona can be sustained by increased diffusion up from the solar photosphere. This is necessarily a loose concept, and so our approach is to calculate the FIP fractionation for open and closed field according to the models outlined above, and then add in

MDF (which arises because the thermal speeds v_{\perp}^2 and $2k_B T/m_k$ are proportional to $1/m_k$, while $v_{||,\text{osc}}^2$ and u_k^2 representing fluid motions are not, and are usually much larger)

$$f_a = \exp \left\{ - \int \frac{dB/dz (v_{\perp}^2/B)}{2k_B T/m_k + v_{||,\text{osc}}^2 + 2u_k^2} dz \right\}, \quad (4)$$

in order to match the isotopic differences between high-speed and low-speed solar wind. The region of integration in Equation (4) is in the corona, out to a heliocentric distance of $1.5\text{--}2 R_{\odot}$, where the corona is sufficiently collisionless in order to allow solar wind acceleration to commence (Cranmer et al. 1999; Miralles et al. 2001). Figure 1 (right panel) shows the resulting fractionations relative to Mg for open (top curves, shifted upwards by 0.5 for clarity) and closed field (bottom). The green lines indicate the effect of the ponderomotive acceleration only, the purple curves show the combined effect of ponderomotive acceleration and the adiabatic invariant conservation. Elements lighter (heavier) than Mg are enhanced (depleted) in abundance by the adiabatic invariant.

Table 1
Isotopic Fractionations

Ratio	Model 1 (Low MDF)	Model 2 (High MDF)	Observations
${}^3\text{He}/{}^4\text{He}$	-4.6%	-5.3%	$6.31 \pm 0.21\%^{\text{l}}$
${}^{20}\text{Ne}/{}^{22}\text{Ne}$	$0.46\% \text{ amu}^{-1}$	$0.41\% \text{ amu}^{-1}$	$0.42 \pm 0.05\% \text{ amu}^{-1\text{a}}$
${}^{36}\text{Ar}/{}^{38}\text{Ar}$	$0.25\% \text{ amu}^{-1}$	$0.20\% \text{ amu}^{-1}$	$0.26 \pm 0.05\% \text{ amu}^{-1\text{a}}$
$f_{\text{FIP,slow}}$	2.69	2.73	2.65 ^b
$f_{\text{FIP,fast}}$	1.91	1.99	2.03 ^b
$B_{\text{freeze,slow}}/B_{\odot}$	0.135 ^c	0.105 ^c	0.094 ^d
$B_{\text{freeze,fast}}/B_{\odot}$	0.368 ^c	0.235 ^c	0.173 ^d

Notes.^a Data from Heber et al. (2012a), slow wind relative to fast wind.^b Pilleri et al. (2015). B field expansions.^c Adjusted to give the best fit to the Ne and Ar isotopic ratios.^d Estimated from Wang & Sheeley (1990).

Figure 2 illustrates some important features of the FIP fractionation in closed loops, based on the chromospheric model of Avrett & Loeser (2008). The top left panel (a) shows the density and temperature structure of the chromosphere. The top middle panel (b) shows chromospheric ionization fractions for low FIP elements, and the top right panel (c) for high FIP elements. The bottom left panel (d) shows the wave energy fluxes in each direction for the three wave frequencies considered, the wave resonant with the coronal loop, and three- and five-minute waves propagating up from the photosphere. The bottom middle panel (e) shows the ponderomotive acceleration (solid line) and the amplitude of slow mode waves induced by the Alfvén wave driver. The bottom right panel (f) shows the fractionations resulting for selected elements relative to Mg. The ponderomotive acceleration has a strong “spike” at an altitude of 2150 km, where the chromospheric density gradient is steep (see the top left panel), resulting in strong fractionation at this height.

3. Results and Discussion

We compare the measured fractionations from *Genesis* samples with models designed to match the solar wind conditions during the *Genesis* period, and seek a “best fit.” In this Letter, as a short cut, we construct individual fast and slow wind models (including the adiabatic invariant), given above in Figure 1 (right panel). These have been tuned to match the observed FIP fractionations given by Pilleri et al. (2015), defined as the sum of the FIP fractionations for Fe, Mg, and Si divided by the sum of those for C, O, and Ne. We assume a time fraction 0.35 during this time period due to fast wind, and 0.65 from slow wind and coronal mass ejections (CMEs), assumed to be similarly fractionated (Pilleri et al. 2015). This then matches the ratio of Mg fluences in fast and slow wind/CMEs, $(0.35f_{\text{FIP,fast}})/(0.65f_{\text{FIP,slow}})$ given by Heber et al. (2014).

Further details of these models are given in Table 1. The assumed diminution of magnetic field, which controls the adiabatic invariant acceleration, is compared to that estimated from Wang & Sheeley (1990). These authors give values for $B_s(R_s)$ at $R_s = 2.5 R_{\odot}$ relative to its value on the solar surface. We estimate the magnetic field decrease at 1.5–2.0 R_{\odot} , where the solar wind decouples collisionally from the Sun to be approximately $\sqrt{B_s(R_s = 2.5 R_{\odot})/B_{\odot}}$, and compare this with

Table 2
Solar N and O Isotopic Abundances

Ratio	Model 1 (Low MDF)	Model 2 (High MDF)	Observations
${}^{16}\text{O}/{}^{18}\text{O}^{\text{a}}$	0.8–0.9	1.57–1.62	2.2 ^b
${}^{25}\text{Mg}/{}^{26}\text{Mg}^{\text{a}}$	0.5–0.8	1.14–1.40	$\simeq 1^{\text{d}}$
${}^{14}\text{N}/{}^{15}\text{N}^{\text{a}}$	0.8–1.0	1.63–1.68	e
${}^{14}\text{N}/{}^{15}\text{N}^{\text{f}}$	455 ^g	452 ^g	$400–714$
			$>500^{\text{h}}$

Notes.^a Fractionation of bulk solar wind relative to photosphere, %/amu; light isotope enriched.^b Data from McKeegan et al. (2011), from *Genesis*.^c Data from Ayres et al. (2013), from spectroscopy.^d Heber et al. (2012b).^e No directly measured photospheric ratio.^f Absolute ratio.^g Calculated from our fractionations, used to correct the *Genesis* measured solar wind ${}^{14}\text{N}/{}^{15}\text{N}$ from Marty et al. (2011).^h Data from Fletcher et al. (2014) for Jupiter and Saturn, respectively.

our assumed model values in Table 1. We assume representative speeds of 450 and 600 km s^{-1} for slow and fast wind, respectively (Pilleri et al. 2015). We emphasize that this magnetic field decrease represents the least constrained free parameter in the model, and is chosen to match existing solar observations, and in combination with the FIP fractionation reproduces data from both *ACE* and *Genesis* simultaneously.

We give two models with differing amounts of MDF corresponding to different magnetic field expansions, $B_{\text{freeze}}/B_{\odot}$, yielding different isotopic fractionations. Both models have been specified to reproduce the observed fractionation between fast and slow wind in ${}^{20}\text{Ne}/{}^{22}\text{Ne}$ and ${}^{36}\text{Ar}/{}^{38}\text{Ar}$, as given in Heber et al. (2012a). The ratio ${}^3\text{He}/{}^4\text{He}$ shows similar behavior that is not accounted for, due to other by now well-known processes involving the resonant absorption of ion-cyclotron waves that arises for ${}^3\text{He}$ alone because of its unusual charge to mass ratio of 2/3. These enhance the ${}^3\text{He}$ abundance (e.g., Bućik et al. 2014) and are currently not included in our model. Table 1 shows that the adjusted model slow-fast wind difference in both Ne and Ar isotopic compositions match well with *Genesis* data.

In Table 2 we compare isotopic fractionations derived by application of Models 1 and 2 to the *Genesis* results with previous inferences in the literature. The modeled fractionations of ${}^{14}\text{N}/{}^{15}\text{N}$, ${}^{16}\text{O}/{}^{18}\text{O}$, and ${}^{25}\text{Mg}/{}^{26}\text{Mg}$ are given for the combined fast and slow, i.e., bulk solar wind observed by *Genesis*, and compared with observations where they exist. Agreement is quite good, with the Sun isotopically lighter than other solar system bodies (compare Ayres et al. 2013). By combining our N model fractionations with the *Genesis* solar wind ${}^{14}\text{N}/{}^{15}\text{N}$ of Marty et al. (2011), we can calculate photospheric ${}^{14}\text{N}/{}^{15}\text{N}$ ratios (Table 2), which can be compared with values for Jupiter and Saturn, often presumed to have formed from the the same pre-solar nebula material accreting the same N_2 as the Sun.

Figure 3 shows the predicted elemental fractionation for bulk (i.e., time integrated) solar wind collected by *Genesis*. The left and right panels give results for Models 1 and 2 as given in Table 1, which have lesser and greater degrees of MDF by conservation of the first adiabatic invariant, respectively. The two models give very similar FIP plots. The symbols in Figure 3 (same in both panels) give the measured *Genesis*

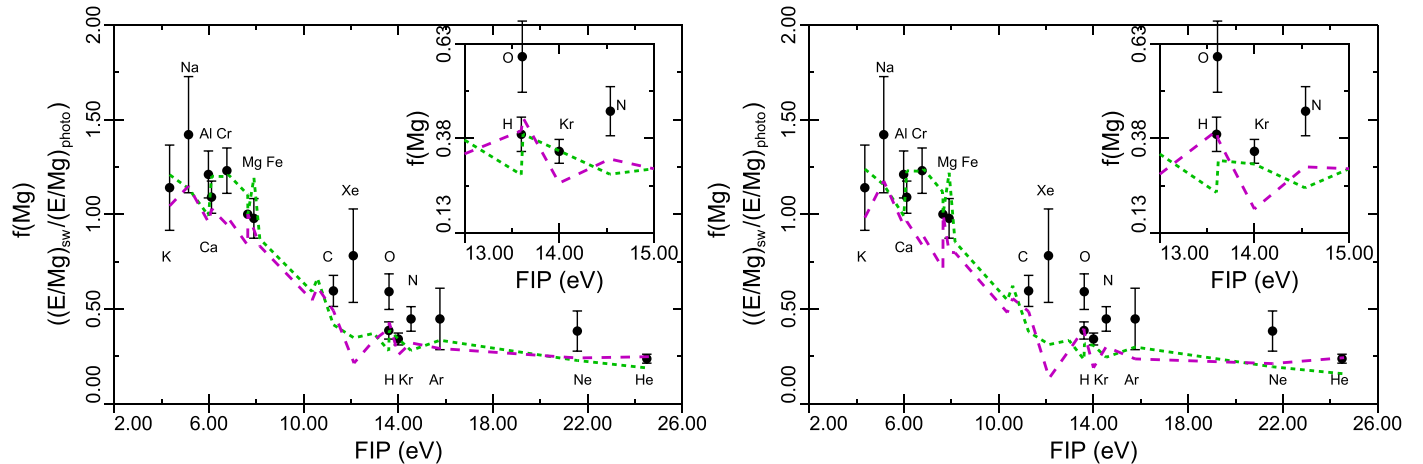


Figure 3. Modeled fractionation patterns for Models 1 (left; low MDF) and 2 (right; high MDF) from Table 1. In each plot, the short dashed green line shows fractionation due to the ponderomotive acceleration alone, and the long dashed purple curve shows the effect of ponderomotive acceleration and adiabatic invariant conservation. Symbols with error bars show results from *Genesis* data analysis. Model 2 assumes a higher mass-dependent fractionation from the adiabatic invariant conservation. Model results for Kr and Xe assume the same ionization balance as for Ar.

fractionations relative to the photospheric abundances of Asplund et al. (2009), Scott et al. (2015a, 2015b), and Grevesse et al. (2015). The *Genesis* results are K, Na, Rieck et al. (2016); Ca, Al, Cr, Heber et al. (2014); Fe, Mg, Jurewicz et al. (2011); C, N, O, Heber et al. (2013); Kr, Xe, Meshik et al. (2014); and H, Koeman-Shields et al. (2016).

The overall agreement between theory and data on Figure 3 is quite good. Inclusion of the adiabatic invariant is a non-negotiable part of the model; it is required to provide the good matches in isotopic ratios shown in Table 1. Exclusion of the adiabatic invariant makes little difference for high FIP elements in Figure 3. The results excluding the adiabatic invariant better match the magnitude of the observed $f(\text{Mg})$ in Figure 3 for the low FIP range between Na and Mg; however, the low FIP trend of the *Genesis* data is better matched by including the adiabatic invariant, but the predicted magnitudes low FIP $F(\text{Mg})$ between Na and Mg are slightly too low relative to the data. Both models predict a small Fe/Mg fractionation that is not present in the data.

Our models are based on fractionations relative to Asplund et al. (2009) as observed with *ACE* by Pilleri et al. (2015). The most accurate *Genesis* data are for Ca, Mg, Fe, H, and He, and we have emphasized the match to these in tuning our models. There are no true photospheric abundances for Ar and Ne; Kr is accurate, but is based on an interpolated CI chondrite solar abundance. As noted, the adiabatic invariant model is only slightly below the low FIP (+C) data. The model agrees well with the high FIP H and He (plus Kr) data; it is distinctly below the O and N points.

The upward displacement of the O and N fractionations above the model curves in Figure 3 may indicate that the photospheric abundances assumed for these elements are too small. The latest revision of CNO photospheric abundances (Asplund et al. 2009; Grevesse et al. 2015; Scott et al. 2015a, 2015b) has recently been challenged by von Steiger & Zurbuchen (2016), who argued that fast solar wind from polar coronal holes is unfractionated and can be used to determine solar metallicity. A solar model based on this composition (Vagozzini et al. 2017) has been criticized by Serenelli et al. (2016). Although fast wind from polar coronal holes can be considerably less fractionated than the fast wind seen in the

ecliptic by *Genesis*, a complete absence of FIP effect is not always supported by coronal hole models of FIP fractionation (Laming 2012, 2015). However, the application of our FIP models to the *Genesis* data analyzed to date supports the conclusion of von Steiger & Zurbuchen (2016), and is also more consistent with higher values obtained previously by Caffau et al. (2008), or even earlier by Grevesse & Sauval (1998).

The minimum amount by which the O abundance should increase to bring the error bar into contact with the model is 0.06–0.14 dex (for Models 1 and 2, respectively), which moves the abundance from 8.69 of Asplund et al. (2009) to 8.75–8.83, in better agreement with Caffau et al. (2008) and/or Grevesse & Sauval (1998). For comparison, Ayres et al. (2013) gave an O abundance of 8.75, and more recently Cubas Armas et al. (2017) gave 8.86 ± 0.04 , both based on spectroscopy.

The error bars on the *Genesis* data are one sigma, thus it is important to await further analyses, especially of low- and high-speed regime samples. The model result is driven by the fast wind model, for which the fractionation ratio $\text{O}/\text{H} < 1$ (see Figure 1(b)), but this is fundamentally a polar coronal hole model applied to fast wind observed in the ecliptic. Measurements of the slow wind abundance ratio O/H would remove this uncertainty. Once this is done, it is possible to achieve a rather complete assessment of the elemental and isotopic composition of the solar photosphere as a proxy for the pre-solar nebula, *by methods completely independent* of those employed to date.

This work was supported by grants from the NASA Heliophysics Supporting Research (NNH16AC39I) and Laboratory Analysis of Returned Samples Programs (NNH17AE60I, NHH15AZ67I, NNX15AG19G) and by basic research funds of the Chief of Naval Research. We are grateful to Yuan-Kuen Ko for discussions of *ACE* data.

ORCID iDs

- J. Martin Laming  <https://orcid.org/0000-0002-3362-7040>
- L. R. Nittler  <https://orcid.org/0000-0002-5292-6089>
- D. B. Reisenfeld  <https://orcid.org/0000-0003-1874-9450>
- J. Wang  <https://orcid.org/0000-0002-7671-2413>

References

- Asplund, M., Grevesse, N., Sauval, A. J., & Scott, P. 2009, *ARA&A*, **47**, 481
- Avrett, E. H., & Loeser, R. 2008, *ApJS*, **175**, 229
- Ayret, T. R., Lyons, J. R., Ludwig, H.-G., Caffau, E., & Wedemeyer-Böhm, S. 2013, *ApJ*, **765**, 46
- Bochsler, P. 2007a, *A&ARv*, **14**, 1
- Bochsler, P. 2007b, *A&A*, **471**, 315
- Bodmer, R., & Bochsler, P. 1998, *A&A*, **337**, 921
- Burnett, D. S. 2013, *M&PS*, **48**, 2351
- Bućik, R., Innes, D. E., Mall, U., et al. 2014, *ApJ*, **786**, 71
- Burnett, D. S., Guan, Y., Heber, V. S., et al. 2017, LPSC, **48**, 1532
- Caffau, E., Ludwig, H.-G., Steffen, M., et al. 2008, *A&A*, **488**, 1031
- Cranmer, S. R., Kohl, J. L., Noci, G., et al. 1999, *ApJ*, **511**, 481
- Cranmer, S. R., & van Ballegooijen, A. A. 2005, *ApIS*, **156**, 265
- Cranmer, S. R., van Ballegooijen, A. A., & Edgar, R. J. 2007, *ApJS*, **171**, 520
- Cubas Armas, M., Asensio Ramos, A., & Socas-Navarro, H. 2017, *A&A*, **600**, A45
- Dahlburg, R. B., Laming, J. M., Taylor, B. D., & Obenschain, K. 2016, *ApJ*, **831**, 160
- De Pontieu, B., McIntosh, S., Carlsson, M., et al. 2007, *Sci*, **318**, 1574
- Fletcher, L. N., Greathouse, T. K., Orton, G. S., et al. 2014, *Icar*, **238**, 170
- Grevesse, N., & Sauval, A. J. 1998, *SSRv*, **85**, 161
- Grevesse, N., Scott, P., Asplund, M., & Sauval, A. J. 2015, *A&A*, **573**, A26
- Heber, V. S., Baur, H., Bochsler, P., et al. 2012a, *ApJ*, **759**, 121
- Heber, V. S., Burnett, D. S., Duprat, J., et al. 2013, LPSC, **44**, 2540
- Heber, V. S., Jurewicz, A. J. G., Janney, P., et al. 2012b, LPSC, **43**, 2921
- Heber, V. S., McKeegan, K. D., Smith, S., et al. 2014, LPSC, **45**, 1203
- Heggland, L., Hansteen, V. H., De Pontieu, B., & Carlsson, M. 2011, *ApJ*, **743**, 142
- Jurewicz, A. J. G., Burnett, D. S., Woolum, D. S., et al. 2011, LPSC, **42**, 1917
- Kasper, J. C., Stevens, M. L., Korreck, K. E., et al. 2012, *ApJ*, **745**, 162
- Koeman-Shields, E. C., Huss, G. R., Ogliore, R. C., et al. 2016, LPSC, **47**, 2800
- Laming, J. M. 2004, *ApJ*, **614**, 1063
- Laming, J. M. 2009, *ApJ*, **695**, 954
- Laming, J. M. 2012, *ApJ*, **744**, 115
- Laming, J. M. 2015, *LRSP*, **12**, 2
- Laming, J. M. 2017, *ApJ*, **844**, 153
- Lynch, B. J., Edmondson, J. K., & Li, Y. 2014, *SoPh*, **289**, 3043
- Marty, B., Chaussidon, M., Wiens, R. C., Jurewicz, A. J. G., & Burnett, D. S. 2011, *Sci*, **332**, 1533
- McKeegan, K. D., Kallio, A. P. A., Heber, V. S., et al. 2011, *Sci*, **332**, 1528
- Meshik, A., Hohenberg, C., Pravdivtseva, O., & Burnett, D. 2014, *GeCoA*, **127**, 326
- Miralles, M. P., Cranmer, S. R., & Kohl, J. L. 2001, *ApJ*, **560**, L193
- Pilleri, P., Reisenfeld, D. B., Zurbuchen, T. H., et al. 2015, *ApJ*, **812**, 1
- Pottasch, S. R. 1963, *ApJ*, **137**, 945
- Rakowski, C. E., & Laming, J. M. , 2012, *ApJ*, **754**, 65
- Rieck, K., Jurewicz, A. J. G., Burnett, D. S., et al. 2016, LPSC, **47**, 2922
- Scott, P., Asplund, M., Grevesse, N., Bergemann, M., & Sauval, A. J. 2015a, *A&A*, **573**, A26
- Scott, P., Grevesse, N., Asplund, M., et al. 2015b, *A&A*, **573**, A25
- Serenelli, A., Scott, P., Villante, F. L., et al. 2016, *MNRAS*, **463**, 2
- Vagozzini, S., Freese, K., & Zurbuchen, T. H. 2017, *ApJ*, **839**, 55
- von Steiger, R., & Zurbuchen, T. H. 2016, *ApJ*, **816**, 13
- Wang, Y.-M., & Sheeley, N. R. 1990, *ApJ*, **355**, 726